Hindawi
International Journal of Aerospace Engineering
Volume 2022, Article ID 4840814, 14 pages
https://doi.org/10.1155/2022/4840814

Research Article

The Reduced-Order Model for Droplet Drift of Aerial Spraying under Random Lateral Wind

Wencheng Li,[1,2] **Wenyun Wang**,[3] **Xiaomao Huang**,[1,2] **and Chenyang Li**[1]

[1]*College of Engineering, Huazhong Agricultural University, Wuhan 430070, China*
[2]*Key Laboratory of Agricultural Equipment in Mid-Lower Yangtze River, Ministry of Agriculture and Rural Affairs, Wuhan 430070, China*
[3]*The 9Th Designing of China Aerospace Science and Industry Corporation, Wuhan 430040, China*

Correspondence should be addressed to Wencheng Li; li_wch@hzau.edu.cn

Received 7 January 2022; Revised 7 March 2022; Accepted 21 March 2022; Published 12 April 2022

Academic Editor: Ti Chen

The droplet drift during aerial spraying process of oilseed rape, which is induced by complex flow field including random lateral wind, is difficult to predict and suppress. In this study, the high-fidelity computational fluid dynamics (CFD) technique is employed to simulate the two-phase flow of droplets in the rotor flow field, and the influence of main operation parameters on spraying effect is investigated numerically. Furthermore, the mechanism of droplet deposition in various operation conditions is discussed according to the analysis of unsteady flow field characteristics. However, the simulation via CFD technique is time-consuming, and it is not suitable for multidisciplinary work and optimization design. To address such issue, a filter white Gaussian noise signal is used to mimic the random lateral wind, and the droplet drift distance is obtained numerically. Based on the input and output dataset of CFD, the recursive algorithm including nonlinear autoregressive exogenous model and surrogate-based recurrence framework and the deep learning method for time-series prediction called long short-term memory neural network are used to build the efficient reduced-order model, respectively. Numerical simulations show that the droplet drift distance can be predicted by measurable lateral wind speed via the reduced-order model approach, which agreed well with the results obtained via the CFD method. In addition, the reduced-order model could decrease computation cost by 6 orders of magnitude with an acceptable accuracy, which indicates that the proposed method could be used for the design of off-line closed-loop controller of a variable spraying system.

1. Introduction

As a most important source of edible oil, oilseed rape is widely planted in mid-lower Yangtze River of China. In addition, different growth stages and various parts of oilseed rape can be processed as vegetable, forage, fertilizer, flower, and honey in an economical way [1, 2]. However, the growth of oilseed rape is seriously affected by pests and diseases, for instance, sclerotia can reduce the yield of oilseed rape crop up to 70% during the blooming period. Considering the limitations of a complex terrain in China, the inefficient traditional ground plant protection machinery cannot satisfy the requirement of plant protection of modern agriculture.

The near-ground aerial spraying based on unmanned aerial vehicle (UAV) flight control and navigation technology, which can operate at high flight speed without the direct touch of crops, provides a feasible and efficient approach [3–6]. Compared with traditional ground plant protection operation, aerial spraying could increase operating efficiency and reduce pesticide consumption. However, the aerial spraying process is a complex gas-liquid-solid interaction system, and the spraying effect is significantly influenced by different operation conditions and environment parameters, such as flight altitude, free-stream velocity, environmental wind field, and nozzle performance [7]. For instance, increasing the flight speed can improve the spraying efficiency but weaken the ability of the downwash to forcing droplets to deposit on the crop surface, making the droplet drift along the downstream direction especially when lateral wind exists [8, 9]. A high flight speed will strengthen

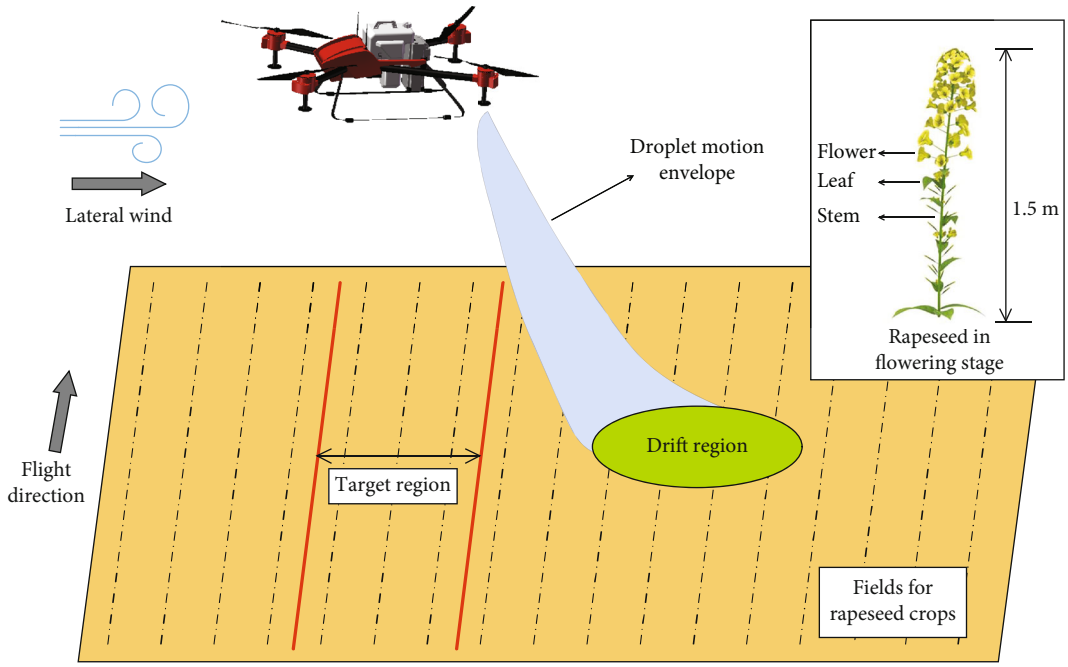

Figure 1: The schematic diagram of oilseed rape aerial spraying.

the coupling effect of vortex and turbulence effect of rotor, leading to the decrease of uniformity, effective range, and density of droplet deposition significantly [10]. Furthermore, the flow field characteristics of downwash near the crop canopy and the droplet spraying uniformity are sensitive to the flight altitude. Based on the computational fluid dynamics (CFD) simulation results for different flight altitudes, it is indicated that as the UAV is far away from the crops, velocity amplitude distribution of the flow field will be more concentrated and the longitudinal velocity gradient of the downwash will be reduced; thus, the wall reflection effect between the downwash flow and crops would be weakened [11]. Wang et al. [8] analyzed the effects of operation altitude and flight speed of UAV on droplet deposition and distribution characteristics; the results indicate that appropriately increasing flight altitude and reducing flight speed had a significant impact on the improvement of spraying effect. Qin et al. [12] investigated the influence of flight parameters of plant protection UAV on droplet drift via experimental method; it is found that the droplet deposition in corn crop canopy could get the ideal operation state when the flight altitude is 7 meters, while the spraying effect is easily affected by downwash flow field and lateral wind at other flight altitudes, which makes a lower penetration and deposition efficiency. In addition, based on the numerical simulation results and wind tunnel experiments, it has been pointed out that the initial velocity direction and droplet trajectory will be changed for various nozzle angles, making a significantly difference in the droplet drift distance along the direction of lateral wind. For instance, the droplet drift distance could be reduced 60% by choosing the proper angle of spraying nozzle when the lateral wind speed reaches 5 m/s [13]. Furthermore, the droplet drift induced by the uncontrollable random lateral wind coupled with the strong periodic downwash flow field of rotor aircraft is difficult to suppress, leading to the waste of pesticide and environmental pollution, which is the most concerned issue to be solved in aerial spraying field. When considering the influence of lateral wind alone, the droplet drift distance and drift rate are linearly related to the amplitude of wind speed. However, when the coupling effect of downwash is taken into account, the lateral wind with small amplitude has limited influence on the droplet drift while a strong lateral wind will significantly increase the droplet drift distance due to the coupled aerodynamic effect of the lateral wind shear and rotor vortex [14].

It can be seen from the above research that the random lateral wind plays an important role in improving the effectiveness and efficiency of aerial spraying. It should be noted that once the desired variable spraying feedback control system is established, the variable-spraying actuator could be automatically operated based on the measured random lateral wind signal to ensure the uniformity of spraying and suppress the droplet drift. However, the construction of control system relies on the high-fidelity CFD method, which is time-consuming especially for the multi-parameter simulation of three-dimensional two-phase flow; thus, it cannot be used in controller design directly [15–17]. To address such issue, the reduced-order model (ROM) technique, which could transform the high-order finite element model into an approximation low-order model, can be used to design the off-line controller in an efficient and accurate way. For instance, based on the system identification theory, Glaz et al. [18] developed the efficient ROM of the rotor to predict the unsteady aerodynamics response via the Kriging surrogate model and surrogate-based recurrence framework. Zhang et al. [19] built the nonlinear ROM of the aeroelastic system in transonic regime by employing the RBF neural

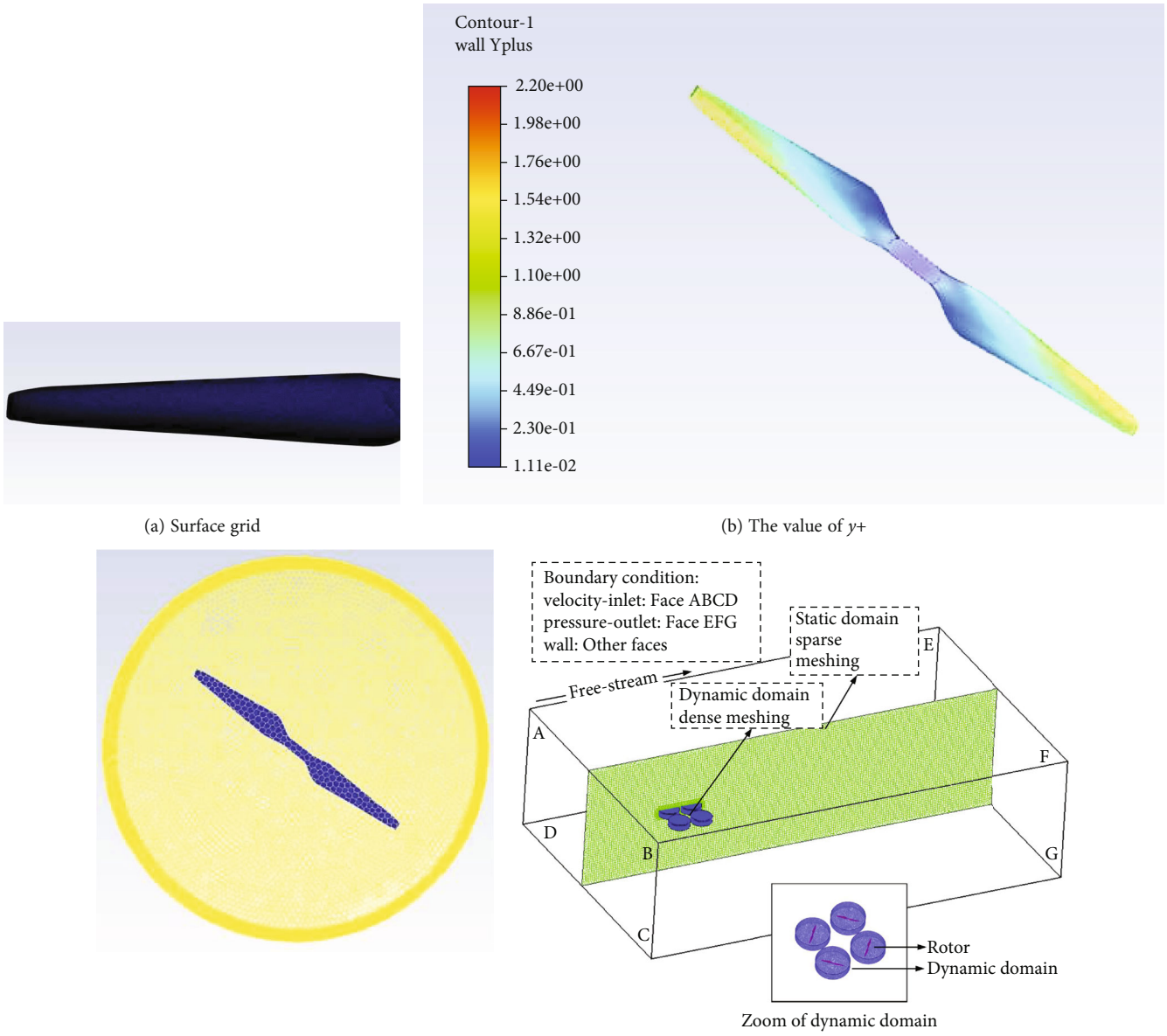

(a) Surface grid

(b) The value of $y+$

(c) Dynamic domain

(d) Overall domain

Figure 2: The mesh grid of computational domain.

network, and the nonlinear dynamics behaviors including limited cycle oscillation and flutter boundary are predicted accurately. Recently, the deep learning method involving long short-term memory (LSTM) neural network has been used to build the ROM of multiple-input-multiple-output fluid-structure interaction system [20, 21]. Based on the integration of the control algorithm and efficient ROM technique, Huang et al. [22] developed the control method for flutter suppression to expand flight envelope via a numerical and experimental technique.

In the process of time-consuming CFD unsteady simulation, the target current output (i.e., droplet deposition) depends mainly on the current input (i.e., the random lateral wind) and previous output. The motivation of this paper is based on the basic principle of CFD unsteady calculation, the reduced-order models are built by employing surrogate-based recurrence framework and deep learning method, respectively, which could predict the current output by the known external input and previous predicted output; thus, the droplet drift response under random lateral wind can be obtained in an efficient way. In what follows, with the consideration of the computational efficiency of multiparameter analysis, a single-rotor model is used to perform the high-fidelity CFD simulation numerically. In particular, the ground is modeled as a conveyor belt, and the droplet deposition characteristics on the ground in forward flight could be presented more accurately and intuitively. Finally, two efficient ROMs are built based on data-driven theory to predict the response of droplet drift. The contributions of this study are as follows: (i) Based on the data obtained via the

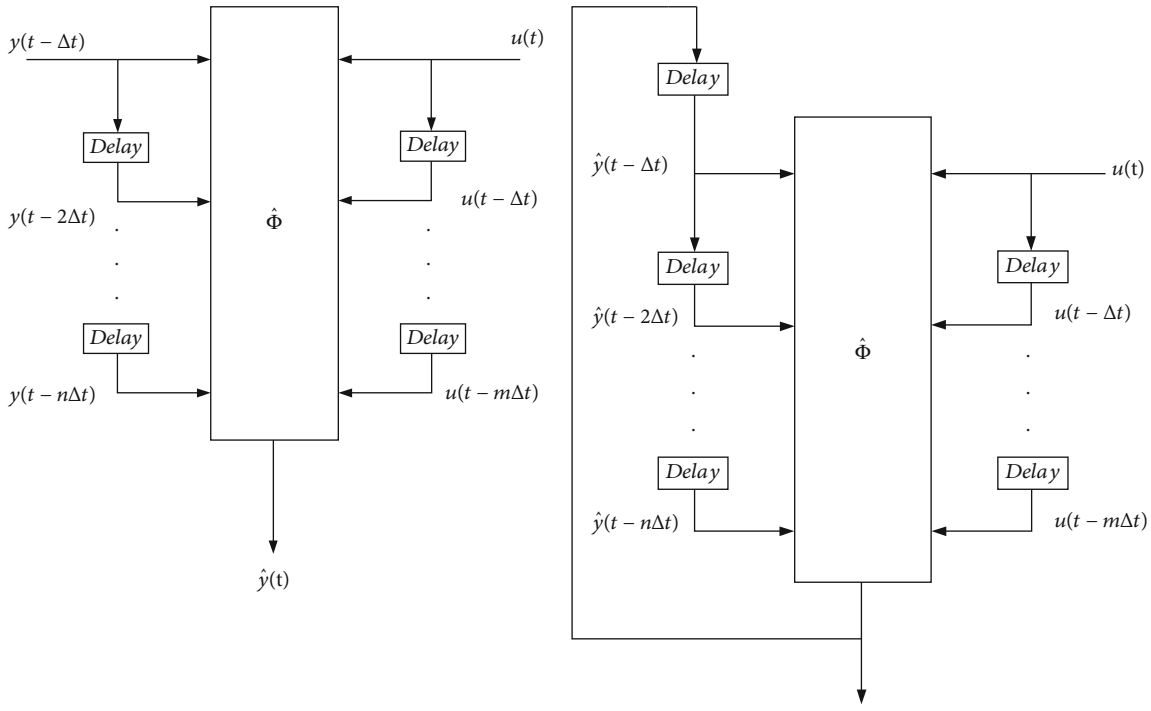

(a) Nonlinear autoregressive exogenous model (b) Surrogate-based recurrence framework

Figure 3: The recurrence scheme for time-series prediction of ROM.

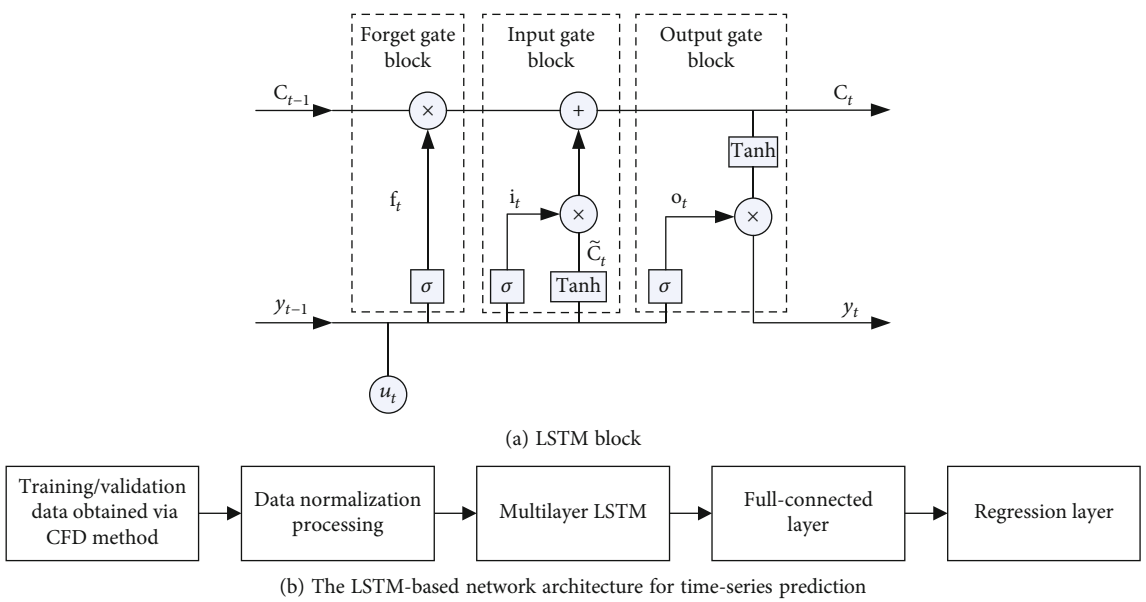

(a) LSTM block

(b) The LSTM-based network architecture for time-series prediction

Figure 4: The LSTM scheme for time-series prediction of ROM.

CFD method, the ground is modeled as a conveyor belt to perform the temporal and spatial distribution characteristic of droplets. (ii) The efficient ROMs are established via the deep learning method and surrogate-based recurrence framework, respectively, to predict the behavior of droplet drift.

The remainder of this study is organized as follows. In Section 2, the simplified finite element model and time-dependent ROM technique based on the recursive algorithm and the LSTM theory are introduced. In Section 3, various simulation cases under different operation conditions are investigated, involving steady and transient situation. In

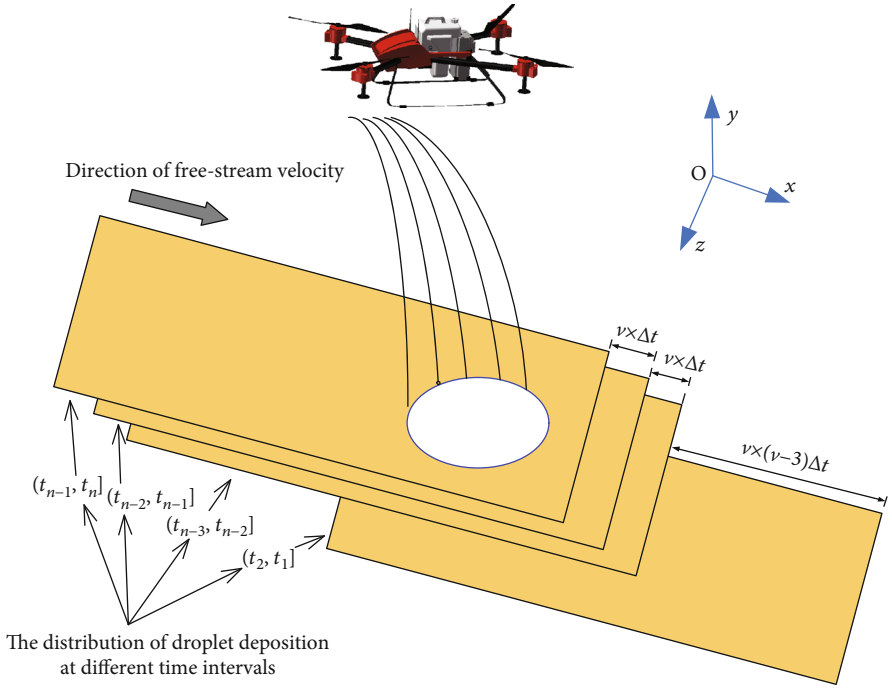

Figure 5: The schematic diagram of conveyor belt model for droplet deposition.

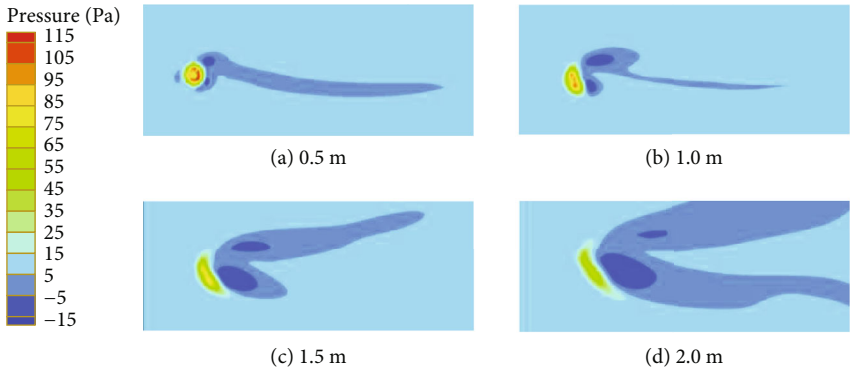

Figure 6: Pressure distribution below the rotor when free stream velocity is 3 m/s.

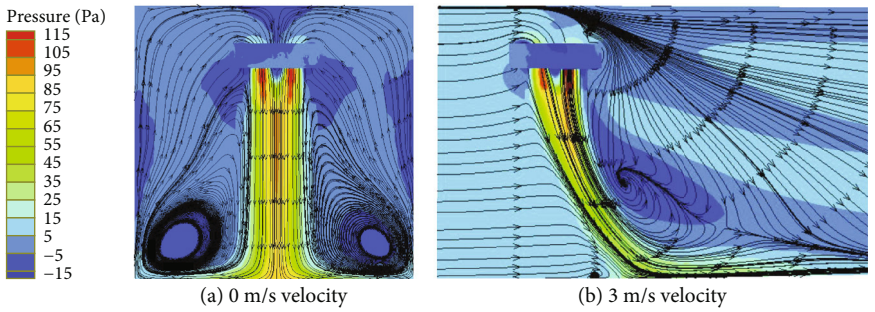

Figure 7: The streamlines of flow field at different free stream velocities.

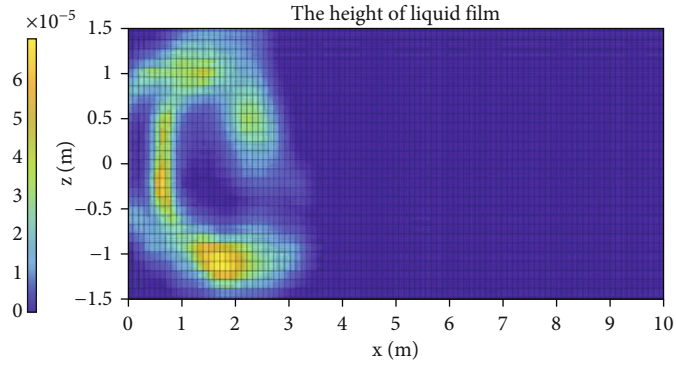

(a) hover state

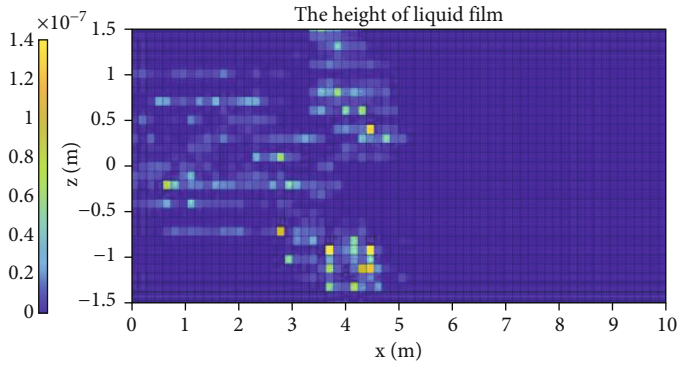

(b) forward flight

Figure 8: The height of deposited liquid film on the ground when velocity is 1 m/s.

addition, the prediction results of ROMs are performed to assess the validity of proposed method. Finally, Section 4 concludes this paper.

2. Background and Theory

2.1. Governing Equation and Simplified Model. The schematic diagram of the oilseed rape aerial spraying system considering the influence of lateral wind is shown in Figure 1, which performs the droplet drift to the nontarget region due to unpredictable meteorological condition. In this study, ignoring the influence of fuselage, the commercial software Fluent is used to analyze the two-phase flow interaction dynamics, and the sliding mesh method is employed to simulate the high-speed rotational motion of the rotor wing. As shown in Equation (1), the governing Navier-Stokes equation can be discretely solved by the second order upwind scheme.

$$\rho \frac{dV}{dt} = f - \nabla p + \mu \nabla^2 V, \tag{1}$$

where ρ is the density of fluid and V, f, and p are the vectors of velocity, external force per unit volume, and pressure, respectively.

To accurately capture the details of the flow field, Euler method and shear stress transfer k-ω turbulence model expressed are chosen to calculate the steady and transient aerodynamic response of the fluid phase. The discrete phase model described via dynamics equation Equation (2) is used to mimic the motion of a discrete phase in the Lagrangian reference frame, where m_p is the mass of particle, u and u_p are the velocity of fluid phase and discrete phase, and ρ and ρ_p denote the density of fluid phase and discrete phase, respectively [23]. $m_p((u - u_p)/\tau_r)$ and F are the drag force and additional force term, respectively, where τ_r is the relaxation time of droplet. It can be seen that the transport of droplet is mainly governed by the initial state of the droplet leaving the nozzle and the aerodynamic load around the rotor.

$$m_p \frac{du_p}{dt} = m_p \frac{(u - u_p)}{\tau_r} + m_p \frac{g(\rho_p - \rho)}{\rho_p} + F. \tag{2}$$

The speed of the rotor and the corresponding time step of transient simulation after steady calculation are set as 2500 rpm and 0.0025 seconds, respectively. Furthermore, a wall-film boundary condition is chosen to capture the deposition and distribution of the droplet on the ground. The surface mesh of rotor wing is presented in Figure 2(a), the hybrid grid is employed to divide the volume mesh, and the total number of grids is about 3.35×10^6, where the diameter and the chord length at 3/4-span location of rotor are 400 mm and 42 mm. The height of the first boundary

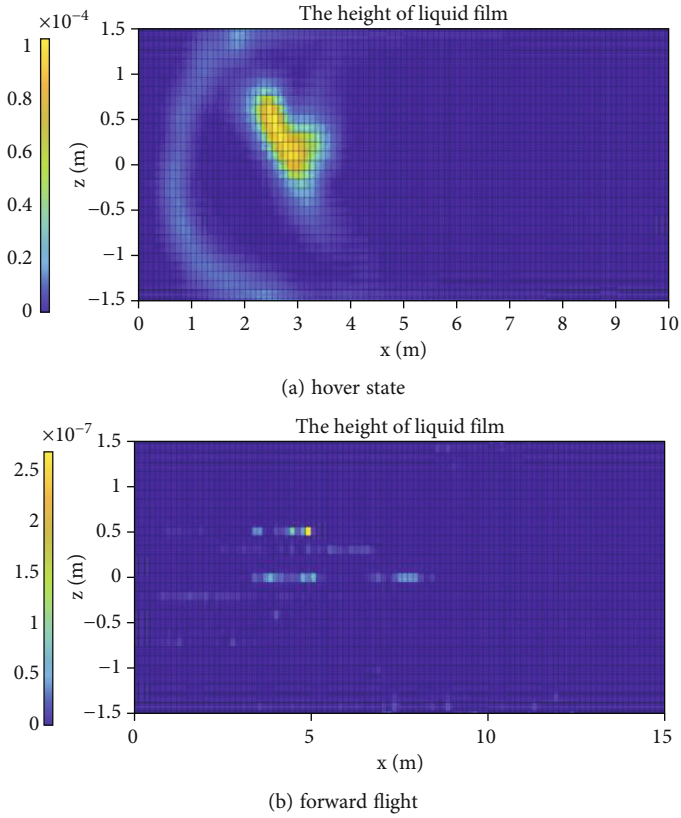

Figure 9: The height of deposited liquid film on the ground when velocity is 2 m/s.

layer is 5×10^{-6} m and the corresponding $y+$ contour is shown in Figure 2(b), which indicates that the volume meshing and boundary layer satisfy the requirement of the chosen turbulence model. The dynamic domain and overall domain are presented in Figures 2(c) and 2(d), respectively, where the diameter and height of dynamic domain are 1032 mm and 400 mm; the size of the overall computation domain is about 26 m × 8 m × 16 m. In order to perform the droplet drift behavior well, the computation domain downstream is larger than the upstream one. The sliding grid method and multiple reference frame (MRF) are employed to model dynamic process of the high-speed rotation of rotor, where the static domain with sparse meshing and dynamic domain with dense meshing are adopted. In addition, a pressure-swirl atomizing hollow cone nozzle is used to generate 200 μm droplets with 0.08 kg/s total flow rate, where the initial velocity of droplets is 35 m/s and the con angle of nozzle is 55 degrees.

2.2. ROMs Based on Recursive Algorithm and LSTM Neural Network

2.2.1. Recursive Algorithm. Based on the time-series prediction method, such as nonlinear autoregressive exogenous model with exogenous inputs Tsungnan et al., [24] and surrogate-based recurrence framework [18] presented in Figure 3, the response of the following multiple-input and multiple-output dynamic system can be predicted, which yields

$$\widehat{y}(t) = \widehat{\Phi}(y(t-1),\cdots,y(t-n), u(t),\cdots,u(t-m)), \tag{3}$$

$$\widehat{y}(t) = \widehat{\Phi}(\widehat{y}(t-1),\cdots,\widehat{y}(t-n), u(t),\cdots,u(t-m)), \tag{4}$$

where Φ is the nonlinear map between the input u and output y and m and n are the time-delay order of input and output, respectively. Superscript $\wedge$ denotes the approximation of corresponding accurate term.

Equations (3) and (4) are black box models based on data-driven of the nonlinear autoregressive exogenous model and surrogate-based recurrence framework, respectively, which can convert a complicated high-order nonlinear system into an approximate low-order model by using the dataset of input and output. It should be noted that the prediction of current output value $\widehat{y}(t)$ via the nonlinear autoregressive exogenous model depends the true value of past output $(y(t-1),\cdots,y(t-n))$, while the prediction of surrogate-based recurrence framework is based on the prediction value of past output dataset $(\widehat{y}(t-1),\cdots,\widehat{y}(t-n))$. However, the true value of output may be difficult or time-consuming to obtain in some situations; thus, the ROM based on surrogate-based recurrence framework provides a feasible approach for such case. In other words, the prediction via surrogate-based recurrence framework-based ROM just needs a well-trained surrogate model $\widehat{\Phi}$ and a real-time measurable input dataset $(u(t),\cdots,u(t-m))$.

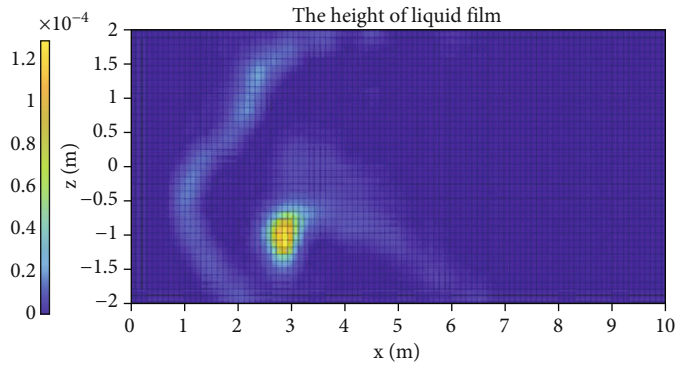

(a) hover state

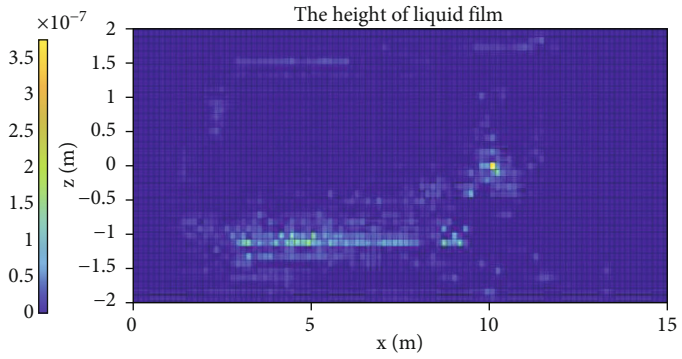

(b) forward flight

Figure 10: The height of deposited liquid film on the ground when velocity is 3 m/s.

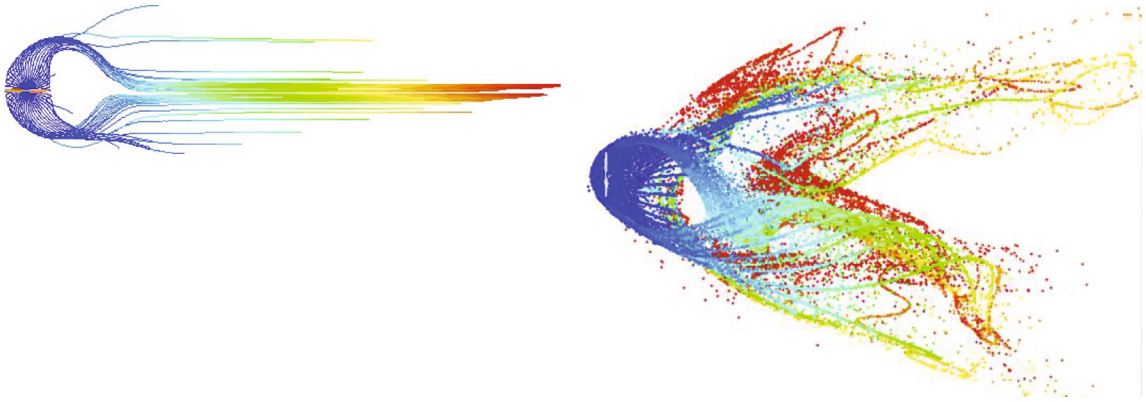

(a) steady state (b) transient state

Figure 11: Droplets trajectory of single-rotor when the free-stream velocity is 3 m/s.

2.2.2. LSTM Neural Network. The LSTM network architecture is presented in Figure 4(a), which consists of three different gates block, namely, forget gate f_t, input gate i_t, and output gate o_t, where the gate function is a Sigmoid function as shown in Equation (5), where W and b are the weight vector and offset term, respectively [25].

$$g(x) = \sigma(Wx + b). \tag{5}$$

When the current input u_t and the previous output storing in state h_{t-1} pass the forget gate, the Sigmoid function in Equation (6) decides whether the signal can pass through the gate. For instance, when the output of the gate function is zero, it is indicated that no information is reserved, whereas the output is 1 represents all signals could pass without barriers. In other words, the gate function suggests the probability of the data passing the block. Similarly, the input gate and output gate are read in Equations (7) and (8), respectively, where W^* and b^* are the corresponding weight vector and offset, respectively.

$$f_t = \sigma\left(W_f \times [y_{t-1}, u_t] + b_f\right), \tag{6}$$

$$i_t = \sigma(W_i \cdot [y_{t-1}, u_t] + b_i), \tag{7}$$

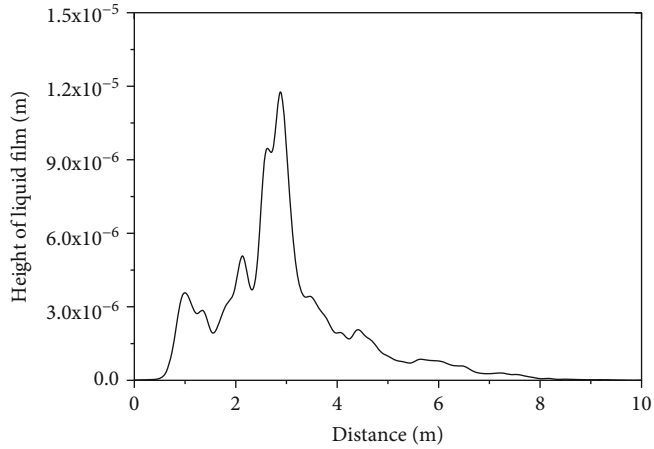

Figure 12: The droplet distribution of a single-rotor model when free stream velocity is 3 m/s.

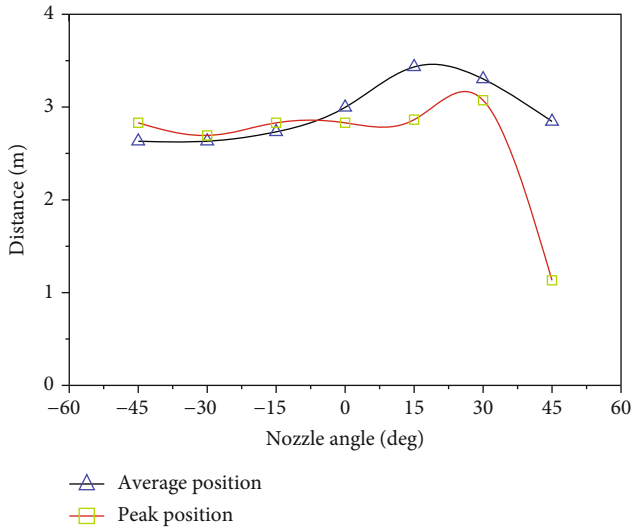

Figure 13: The drift distance for different nozzle angles in hover state when velocity is 3 m/s.

$$o_t = \sigma(W_o \cdot [y_{t-1}, u_t] + b_o). \tag{8}$$

In addition, the candidate memory cell $\tilde{C}_t$ with a tanh function is used to map the input u_t and the previous output state h_{t-1} to the interval $[-1, 1]$, as shown in Equation (9). Afterwards, the current memory cell state C_t can be obtained via Equation (10), which is used to store the long-term state automatically based on the forget gate f_t and input gate i_t. Finally, the output response h_t is calculated by the output gate o_t and the tanh map of memory cell state C_t, which yield Equation (11).

$$\tilde{C}_t = \tanh\left(W_{\tilde{C}} \cdot [y_{t-1}, u_t] + b_c\right), \tag{9}$$

$$C_t = f_t * C_{t-1} + i_t * \tilde{C}_t, \tag{10}$$

$$y_t = o_t * \tanh\left(C_t\right). \tag{11}$$

A multilayered LSTM neural network is employed to improve the generalization performance, and the network architecture for time-series prediction is presented in Figure 4(b) [21]. It should be pointed out that the test and prediction process of the LSTM neural network can be performed without the true output dataset, which is the same as the surrogate-based recurrence framework-based ROM.

3. Case Study and Discussion

3.1. The Droplet Drift through Time. The droplet deposition at different moments in the hover state can be obtained via the CFD method directly, and the desired droplet distribution in target area through time can be calculated approximately via the stack of deposition response at each moment, as shown in Figure 5. Let the velocity of free-stream be constant v, and the droplet distribution through time $\varphi_{\text{through time}}$ can be calculated, which yields,

$$\varphi_{\text{through time}} = \varphi_N(x, z, t_N) + \varphi_{N-1}(x + v \cdot \Delta t, z, t_{N-1}) + \cdots + \varphi_1(x + v \cdot (N-1)\Delta t, z, t_1), \tag{12}$$

where φ_k is the droplet distribution that moved along the free stream direction at different time intervals, which can be calculated by the following CFD simulation results.

$$\varphi_k(x, z, t_k) = \Phi_{k+1}(x, z, t_{k+1}) - \Phi_k(x, z, t_k), \tag{13}$$

where $\Phi_k(x, z, t_k)$ is the function of droplet distribution deposited on the ground directly obtained via the CFD method at the corresponding time k.

3.2. The Characteristics of Single-Rotor Model. To investigate the transport and deposition mechanism of droplet, the pressure contours of flow field at different heights are obtained as shown in Figure 6, where the velocity of free stream is 3 m/s, and the rotor is 3 meters above ground. It can be seen that a high-pressure area is located below the rotor, and a region of low-pressure behind the rotor is generated along the direction of free stream, forcing the droplet to move and deposit downstream under the coupled effect of

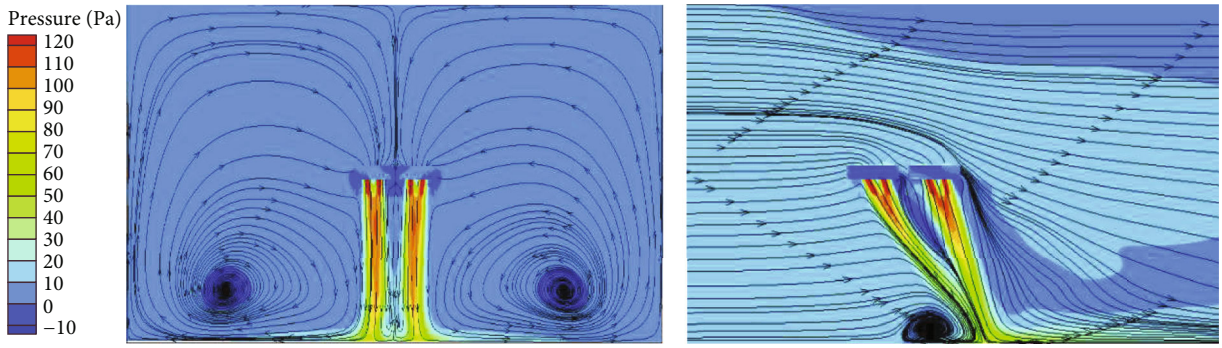

(a) Hover state (b) Flight state at 3m/s

Figure 14: The streamlines of quadrotor flow field.

gravity. In addition, with the increase of the distance from the rotor, the pressure gradient is reduced while the region of low-pressure is enlarged, which may contribute to the drift and transport of droplet near ground. The streamlines of flow field in hover state and flight state with 3 m/s free stream velocity are presented in Figure 7, it can be seen that the characteristics of the flow field, especially the distribution and strength of the vortex structure, are seriously affected by the free stream velocity.

The droplet depositions for various velocities are performed in Figures 8–10, and the top views of droplets trajectory including steady and transient solution when lateral wind velocity is 3 m/s are presented in Figure 11. The simulation results are consistent with the conclusion of flow field analysis performed in Section 3.2. In Figures 8–10, the hover state represents the rotor is hovering and the lateral wind velocity is considered, and the forward flight state means the rotor maintains horizontal flight with a given velocity. It can be found in the simulation of hover state that the peak location of droplet deposition will move downstream with the increase of lateral wind speed.

By changing the initial state of the droplet leaving, the nozzle and variable spraying parameters, such as spraying pressure and nozzle angle, could be used to control the movement and distribution of droplet. The distribution of droplet along the lateral wind direction in the hover state is presented in Figure 12, where the nozzle angle is zero and lateral wind velocity is 3 m/s, and it is indicated that the peak location is about 3 m from the center of rotor and the drift distance is 8 m to 10 m. For various nozzle angles, the distribution distance of droplet in hover state is presented in Figure 13; the negative and positive nozzle angle represents the deflections against and along the lateral wind direction, respectively. The average position $\bar{x}$ is calculated by Equation (14) as follows, where H_i and x_i are the height of liquid film and corresponding position of each grid cell. It can be found that there is little difference for the cases of negative nozzle angle between peak position and average position, while the gap of peak position and average position is enlarged when the nozzle angle is positive especially at 45 deg. In addition, compared with the average position, the peak position is more sensitive to the nozzle angle.

$$\bar{x} = \frac{\sum_{i=1}^{N}(H_i x_i)}{\sum_{i=1}^{N}(H_i)}. \tag{14}$$

3.3. The Characteristics of Quadrotor Model. For the quadrotor model, the steady cases with different velocities of free stream are simulated, which could provide accurate initial value for transient calculation. The height of the rotor from the ground is fixed at 3 m, the coordinates of the rotor center on the horizontal plane are (0, 0), (0, 1.5 m), (1.5 m, 0), and (1.5 m, 1.5 m), respectively. The streamlines of both hover state and forward flight state, which is under the background of total pressure, are presented in Figure 14. It should be noted that, with the near-ground vortex formed around the rotor in the hover state, the flow field structure especially the position and strength of the vortex structure in a forward flight state can be changed significantly by a slight velocity perturbation so that the movement of small and light droplets will be obviously different for various aerodynamic loads.

The trajectory of droplets under steady state with 3 m/s free stream velocity is performed in Figure 15(a). Furthermore, due to the effect of air curtain formed by the rotor flow field, the droplets drift farther along the outside. Based on the steady results, the transient cases are calculated numerically to perform the dynamic process of droplet migration. Figure 15(b) is the transient state of aerial spraying with the velocity of free stream 3 m/s, and it can be found that the drift distance along the lateral direction is much wider than that obtained via steady simulation.

Based on the wall-film boundary condition of the ground, the droplet deposition in the target area can be obtained. For instance, Figure 16 is the droplet distribution on the ground along the direction of free stream, where the nozzle angle is zero and lateral wind velocity is 3 m/s, and it indicates that the peak location is near about 3 meters away from the rotor, which performs a similar deposition distribution characteristic of a single-rotor model shown as Figure 12. In addition, for both the single-rotor model and quadrotor model, the average droplet drift distances defined

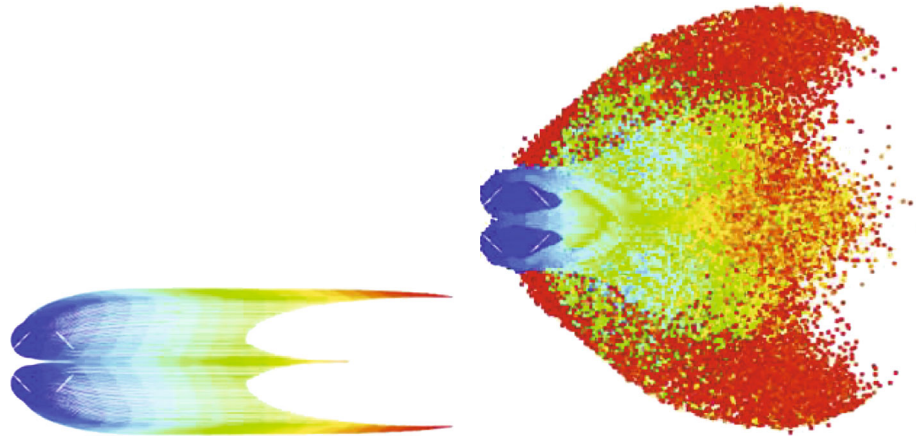

(a) steady state (b) transient state

Figure 15: Droplets trajectory of a quadrotor model when the free stream velocity is 3 m/s.

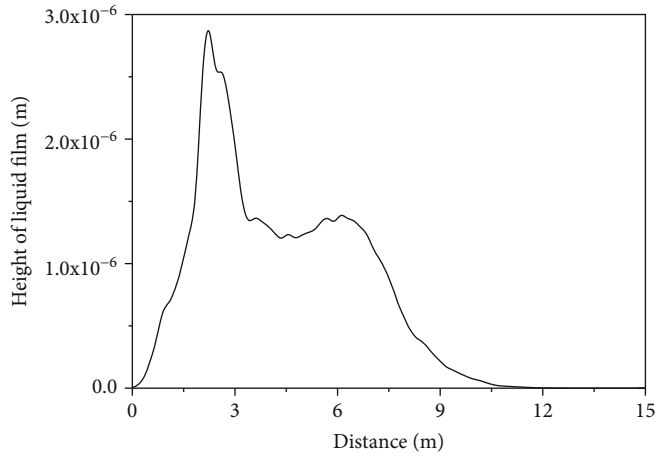

Figure 16: The droplet distribution of quadrotor model when free stream velocity is 3 m/s.

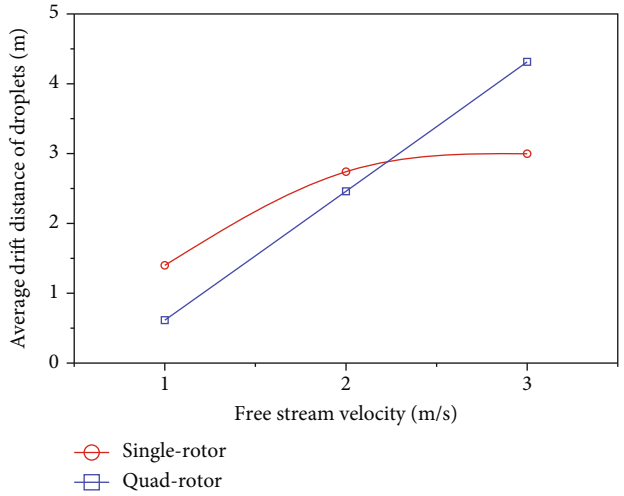

Figure 17: The average drift distance of droplets for different free stream velocities.

as Equation (14) are performed in Figure 17. It can be easily found that the average position of quadrotor model increases approximately linearly with the velocity of free stream, while the average position of single-rotor model increases nonlinearly, which indicates that the droplets deposition characteristics of a single-rotor model is more complicated.

3.4. The Droplet Drift due to Random Lateral Wind. Based on the analysis of flow field and droplet drift for various velocities in the above section, it is implied that the drift distance and distribution of droplets are closely related to lateral wind velocity. It should be noted that to obtain a sufficient amount of computational data with less computing resources, the single-rotor model is used to generate the high-fidelity output data. In addition, to mimic the random lateral wind in the real operation environment, a filter white Gaussian noise signal with 2.5 m/s mean value and low frequency presented in Figure 18 is employed to simulate the value of random lateral wind, which can be obtained via a

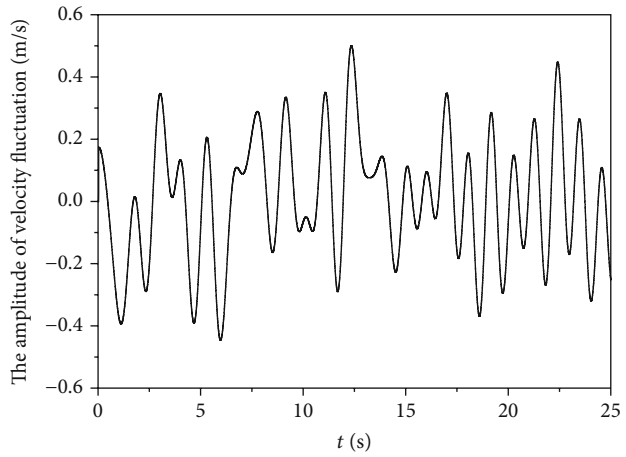

Figure 18: The signal for fluctuation of random lateral wind with 2.5 m/s mean value.

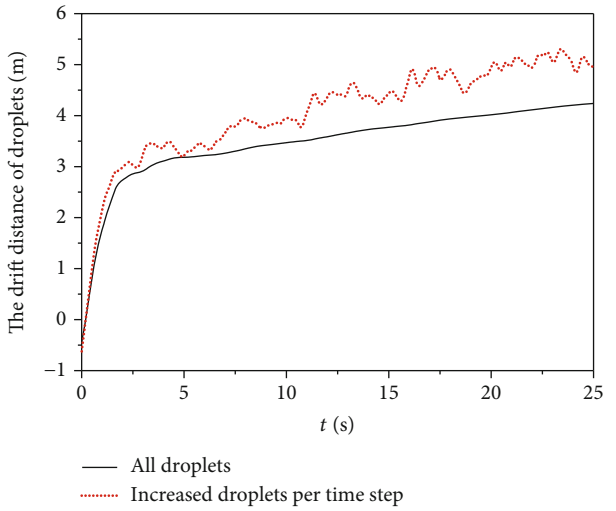

Figure 19: Droplet drift distance with the consideration of random lateral wind.

sum of finite number of harmonic function, namely [26],

$$v(t) = \sum_{i=1}^{100} \bar{v}_i \cos\left(\omega_{v,i} t + \phi_{v,i}\right), \tag{15}$$

where v is the velocity of random lateral wind and $\omega_{v,i}$ and $\phi_{v,i}$ are angular frequency and phase, respectively. The random lateral wind signal can be described by the user-defined function tool in Fluent software, which is compiled with C language and loaded as a boundary condition automatically.

Afterwards, the simulation with 10^4 timesteps in 25 seconds is performed to study the aerial spraying in hover state, and the drift distance between droplet and rotor is presented in Figure 19, where the straight line is the average drift distance of all droplets obtained from Equation (14), and the dot one represents the average drift distance of increased droplets in each time interval. As shown in Figure 19, it takes about 2.5 seconds for the droplets to reach the ground, then the drift distance of all droplets increases linearly approximately, while the drift distance of increased droplets is markedly changed with the variation of random lateral wind signals. It should be noted that the high-fidelity CFD calculation for the corresponding response of droplet which is subject wind load is time-consuming, i.e., it takes about 1.54×10^6 seconds for the transient calculation of Figure 18 (the computer platform is i7 8700k with 6 cores @3.7 GHz and 40 Gb 2400 MHz memory).

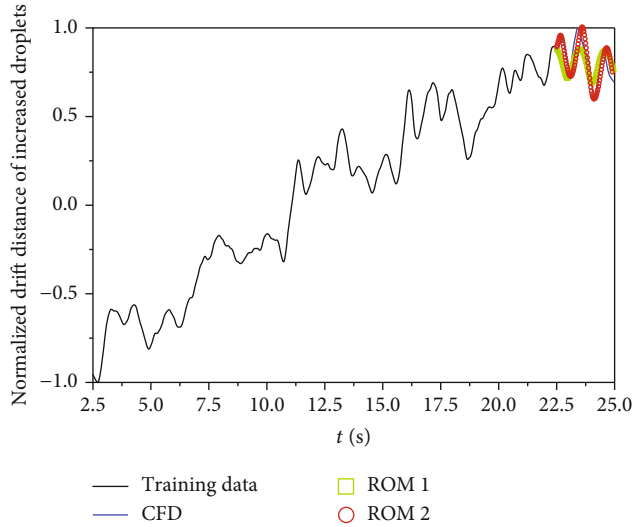

Figure 20: The training and prediction for the drift distance of increased droplets.

3.5. The Prediction of Droplet Drift via Surrogate-Based Recurrence Framework and LSTM. To predict the drift distance of droplets with the consideration of random lateral wind efficiently and accurately, the LSTM network and surrogate-based recurrence framework are used to establish the ROM, respectively, where the normalized data belong to [2.5 s, 22.5 s] and [22.5 s, 25 s] are the training and test datasets, respectively.

In the ROM based on the LSTM neural network, a two-stacked-layer structure with 32 cells in each layer is employed, and mean absolute error function is taken as the error function. In addition, the value of learning rate is given as 0.001 and the Adam optimizer is chosen to complete a 200-epoch training process [27].

In the ROM based on the recursive algorithm, the nonlinear autoregressive exogenous model is used to process the training process, where the number of neurons and is 24, and the delay order $m = n = 1$. The Bayesian regularization algorithm, which can result in good generalization for difficult, small, or noisy datasets, is employed to perform the training process [28]. In the test process, based on the measurable random lateral wind signal, the prediction for the response of aerial spraying system is performed via the surrogate-based recurrence framework without the true output dataset.

The prediction results are presented in Figure 20, and it can be seen that both of the proposed ROMs could

predict the trend of drift distance well, especially the ROM based on the surrogate-based recurrence framework scheme, where ROM 1 and ROM 2 are obtained via LSTM and surrogate-based recurrence framework, respectively. It should be noted that, due to the randomness of droplet motion and high time delay between the instantaneous loading of random lateral wind and droplet deposition, the difficulty of establishing efficient ROM is intensified significantly. In addition, the prediction accuracy of ROM could be further improved by increasing the scale of training data obtained from CFD technique. Furthermore, although it is time-consuming to obtain the training and test datasets via CFD technique, it only takes a fraction of one second to accurately predict the droplet response once the ROM is established. The efficient ROM has potential in designing the close-loop controller for a variable spraying system, which has been applied in fluid-structure interaction system successfully.

4. Conclusions

In this study, the droplet drift of the aerial spraying for various parameters including free-stream velocity, nozzle angle, and random lateral wind are performed numerically, and the distributions of droplets through time for different velocities are calculated to present the overall details. Finally, the efficient ROMs based on the LSTM neural network and surrogate-based recurrence framework are developed, respectively, to predict the droplet drift distance according to the measurable random lateral wind. The CFD data is employed to assess the effectiveness, and the following conclusions can be obtained:

(1) The distributions of droplet can be changed significantly for different nozzle angles, which could be treated as one of the variable spraying parameters

(2) The droplet drift is very sensitive to the wind velocity, in other words, a relatively huge difference of drift distance will be made by a small change of wind velocity

(3) The ROM technique based on surrogate-based recurrence framework and LSTM neural network can be used to predict the droplet drift distance induced by random lateral wind accurately with a low computational cost

Data Availability

All data included in this study are available upon request by contact with the corresponding author.

Conflicts of Interest

The authors declare that they have no known competing interests.

Acknowledgments

This work was supported by the National key research and development program of China (2021YFD1600503), Natural Science Foundation of Hubei Province of China (2020CFB309), and the Key Research and Development Program of Hubei Province of China (2020BBB062).

References

[1] X. Huang, S. Zhang, C. Luo, W. Li, and Y. Liao, "Design and experimentation of an aerial seeding system for rapeseed based on an air-assisted centralized metering device and a multi-rotor crop protection UAV," *Applied Sciences*, vol. 10, no. 24, p. 8854, 2020.

[2] X. Lei, Y. Liao, Q. Zhang, L. Wang, and Q. Liao, "Numerical simulation of seed motion characteristics of distribution head for rapeseed and wheat," *Computers and Electronics in Agriculture*, vol. 150, pp. 98–109, 2018.

[3] F. Ahmad, B. Qiu, X. Dong et al., "Effect of operational parameters of UAV sprayer on spray deposition pattern in target and off-target zones during outer field weed control application," *Computers and Electronics in Agriculture*, vol. 172, article 105350, 2020.

[4] Q. Guo, Y. Zhu, Y. Tang et al., "CFD simulation and experimental verification of the spatial and temporal distributions of the downwash airflow of a quad-rotor agricultural UAV in hover," *Computers and Electronics in Agriculture*, vol. 172, article 105343, 2020.

[5] K. Li, J. Kou, and W. Zhang, "Deep neural network for unsteady aerodynamic and aeroelastic modeling across multiple Mach numbers," *Nonlinear Dynamics*, vol. 96, no. 3, pp. 2157–2177, 2019.

[6] C. Song, Z. Zhou, Y. Zang et al., "Variable-rate control system for UAV-based granular fertilizer spreader," *Computers and Electronics in Agriculture*, vol. 180, article 105832, 2021.

[7] J. Li, Y. Lan, and Y. Shi, "Research progress on airflow characteristics and field pesticide application system of rotary-wing UAV," *Transactions of the Chinese Society of Agricultural Engineering*, vol. 34, pp. 104–118, 2018, (In Chinese).

[8] C. Wang, J. Song, X. He, Z. Wang, S. Wang, and Y. Meng, "Effect of flight parameters on distribution characteristics of pesticide spraying droplets deposition of plant-protection unmanned aerial vehicle," *Transactions of the Chinese Society of Agricultural Engineering*, vol. 33, pp. 109–116, 2017, (In Chinese).

[9] C. Wang, X. He, X. Wang et al., "Distribution characteristics of pesticide application droplets deposition of unmanned aerial vehicle based on testing method of deposition quality balance," *Transactions of the Chinese Society of Agricultural Engineering*, vol. 32, pp. 89–97, 2018, (In Chinese).

[10] M. Lv, S. Xiao, Y. Tang, and Y. He, "Influence of UAV flight speed on droplet deposition characteristics with the application of infrared thermal imaging," *International Journal of Agricultural and Biological Engineering*, vol. 12, pp. 10–17, 2019.

[11] Y. Zheng, S. Yang, X. Liu et al., "The computational fluid dynamic modeling of downwash flow field for a six-rotor UAV," *Frontiers of Agricultural Science and Engineering*, vol. 5, no. 2, pp. 159–167, 2018.

[12] W. Qin, B. Qiu, X. Xue, C. Chen, Z. Xu, and Q. Zhou, "Droplet deposition and control effect of insecticides sprayed with an

unmanned aerial vehicle against plant hoppers," *Crop Protection*, vol. 85, pp. 79–88, 2016.

[13] Y. Chen, C. Hou, Y. Tang, J. Zhuang, J. Lin, and S. Luo, "An effective spray drift-reducing method for a plant-protection unmanned aerial vehicle," *International Journal of Agricultural and Biological Engineering*, vol. 12, no. 5, pp. 14–20, 2019.

[14] J. Wang, Y. Lan, H. Zhang et al., "Drift and deposition of pesticide applied by UAV on pineapple plants under different meteorological conditions," *International Journal of Agricultural and Biological Engineering*, vol. 11, no. 6, pp. 5–12, 2018.

[15] S. Wen, J. Han, Z. Ning et al., "Numerical analysis and validation of spray distributions disturbed by quad- rotor drone wake at different flight speeds," *Computers and Electronics in Agriculture*, vol. 166, article 105036, 2019.

[16] S. Wen, N. Shen, J. Zhang et al., "Single-rotor UAV flow field simulation using generative adversarial networks," *Computers and Electronics in Agriculture*, vol. 167, article 105004, 2019.

[17] B. Zhang, Q. Tang, L. Chen, R. Zhang, and M. Xu, "Numerical simulation of spray drift and deposition from a crop spraying aircraft using a CFD approach," *Biosystems Engineering*, vol. 166, pp. 184–199, 2018.

[18] B. Glaz, L. Liu, and P. P. Friedmann, "Reduced-order nonlinear unsteady aerodynamic modeling using a surrogate-based recurrence framework," *AIAA Journal*, vol. 48, no. 10, pp. 2418–2429, 2010.

[19] W. Zhang, B. Wang, Z. Ye, and J. Quan, "Efficient method for limit cycle flutter analysis Based on nonlinear aerodynamic reduced-order models," *AIAA Journal*, vol. 50, no. 5, pp. 1019–1028, 2012.

[20] J. Li, Y. Shi, Y. Lan, and S. Guo, "Vertical distribution and vortex structure of rotor wind field under the influence of rice canopy," *Computers and Electronics in Agriculture*, vol. 159, pp. 140–146, 2019.

[21] W. Li, X. Gao, and H. Liu, "Efficient prediction of transonic flutter boundaries for varying Mach number and angle of attack via LSTM network," *Aerospace Science and Technology*, vol. 110, article 106451, 2021.

[22] R. Huang, H. Liu, Z. Yang, Y. Zhao, and H. Hu, "Nonlinear reduced-order models for transonic aeroelastic and aeroservoelastic problems," *AIAA Journal*, vol. 56, no. 9, pp. 3718–3731, 2018.

[23] A. D. Gosman and E. Loannides, "Aspects of computer simulation of liquid-fueled combustors," *Journal of Energy*, vol. 7, no. 6, pp. 482–490, 1983.

[24] T. Lin, B. G. Horne, P. Tino, and C. L. Giles, "Learning long-term dependencies in NARX recurrent neural networks," *IEEE Transactions on Neural Networks*, vol. 7, no. 6, pp. 1329–1338, 1996.

[25] S. Hochreiter and J. Schmidhuber, "Long short-term memory," *Neural Computation*, vol. 9, no. 8, pp. 1735–1780, 1997.

[26] D. E. Raveh, "Identification of computational-fluid-dynamics based unsteady aerodynamic models for aeroelastic analysis," *Journal of Aircraft*, vol. 41, no. 3, pp. 620–632, 2004.

[27] Z. Zhang, "Improved Adam optimizer for deep neural networks," in *2018 IEEE/ACM 26th International Symposium on Quality of Service*, Banff, AB, Canada, 2018.

[28] F. Burden and D. Winkler, *Bayesian Regularization of Neural Networks. Artificial Neural Networks: Methods and Applications*, Humana press, Totowa, NJ, 2009.